Journal of Magnetic Resonance 309 (2019) 106602

Contents lists available at ScienceDirect

Journal of Magnetic Resonance

journal homepage: www.elsevier.com/locate/jmr

Low-distortion diffusion tensor MRI with improved phaseless encoding

Rui Tian *, Franciszek Hennel, Klaas P. Pruessmann

Institute for Biomedical Engineering, ETH Zurich and University of Zurich, Zurich, Switzerland

ARTICLE INFO

Article history:
Received 18 June 2019
Revised 13 September 2019
Accepted 16 September 2019
Available online 17 September 2019

Keywords:
MRI
Super-resolution
Phaseless encoding
Diffusion tensor imaging

ABSTRACT

Due to the motion-related instability of the signal phase, diffusion MRI is usually performed with single-shot techniques such as the echo-planar imaging (EPI), which are resolution-limited and suffer from distortions caused by resonance offsets. Multi-shot methods may improve the images but require time-consuming navigators or a trade-off of the sensitivity encoding to measure shot-dependent phase errors. We have recently introduced an alternative approach to multi-shot MRI called phaseless encoding, which, by analogy to optical super-resolution methods, relies on the magnitude value of images taken in different shots thus discarding the phase error without navigators, and demonstrated its capability to perform diffusion MRI at sub-millimeter scale on a standard 3T scanner.

In this work, we apply phaseless encoding in a routine diffusion tensor imaging (DTI) protocol with a moderately high resolution that is still within reach of single-shot EPI with the same hardware, and compare both techniques with respect to image distortions. A qualitative comparison of the phaseless encoding with the established navigator-based readout-segmented EPI is also presented. Several technical improvements are proposed to make phaseless encoding compatible with the routine scanning mode. The tagging radiofrequency pulses used in the encoding sequence are made slice-selective to avoid artefacts caused by saturation effects in multi-slice scans and their flip angle is optimized to reduce the intrinsic SNR loss. The super-resolution reconstruction algorithm is also improved to better suppress Gibbs ringing and to correct for possible signal amplitude fluctuations. Our study shows that the phaseless encoding is a promising approach to diffusion weighted imaging. It can easily be implemented in multi-slice sequences and produces less distorted images than the single-shot EPI at the same resolution and hardware parameters. It provides similar results to readout-segmented EPI but without the need of navigators.

1. Introduction

Diffusion weighted- (DW) and diffusion tensor imaging (DTI) are usually performed with single shot MRI techniques such as the Echo Planar Imaging [1] due to the sensitivity of the signal phase to microscopic motion introduced by diffusion-sensitizing gradient pulses [2]. Consequently, the resolution of most DTI studies is moderate compared to other MRI applications and usually does not surpass 2 mm for the human head, which is dictated by the capabilities of single shot EPI with typical gradient systems. Pushing the resolution higher with this technique increases image distortions due to the inhomogeneity of the magnetic field and requires image corrections based on additional scans of the magnetic field map [3], duplicated EPI scans with inverted image distortions [4] or high parallel acceleration factors with the related SNR tradeoff [5]. A well-known way to increase the resolution of EPI without the distortion penalty is to split the scan to several interleaved [6] or shifted [7–9] segments. However, the motion-related phase instability mentioned before makes this approach extremely challenging. Multi-shot diffusion EPI has been successfully demonstrated only with the use of navigators [9–11] or with a sufficient margin of coil sensitivity information left for the phase correction rather than the sampling acceleration [12–14].

We have recently demonstrated an alternative approach to multi-shot DTI that is based on the so-called phaseless encoding [15,16], i.e. on a series of low-resolved scans prepared by a microscopic sinusoidal tagging sequence with different shifts [17]. The tag is produced by a pair of RF pulses with flip angle α and a relative phase shift $\pi - \Psi$ separated by a gradient pulse in the direction of the encoding (x), which produces a sinusoidal modulation pattern of the z-magnetization

$$A\cos(kx + \Psi) + 1 - A \quad (1)$$

* Corresponding author at: Institute for Biomedical Engineering, Gloriastrasse 35, 8092 Zurich, Switzerland.
E-mail address: rtian@student.ethz.ch (R. Tian).

https://doi.org/10.1016/j.jmr.2019.106602
1090-7807/

where A = $\sin^2\alpha$ and k is the k-space step produced by the gradient pulse. When the magnetization so prepared is used for an imaging sequence, the signal $S(k_x, k_y)$ is convolved with the spectrum of the tagged pattern and contains three shifted components:

$$\frac{A}{2}e^{-i\Psi}S(k_x - k, k_y) + (1 - A)S(k_x, k_y) + \frac{A}{2}e^{i\Psi}S(k_x + k, k_y) \quad (2)$$

When this encoding is applied to EPI, where the k-space trajectory covers one band along the phase encoding direction (y), the two additional signal components provide information from side bands and give a potential resolution enhancement in the readout direction (x) by a factor of three. In practice, the shift k is adjusted to give a slight band overlapping and a slightly lower super-resolution factor. The experiment has to be acquired with at least three different shifts to solve for the contributions of the three bands.

This method is inspired by the structured illumination super-resolution microscopy [18–20] and, like its optical analogue, accepts magnitude images at the input of the reconstruction algorithm. The problematic phase fluctuations caused by the diffusion-weighting are thus discarded in a straightforward manner by taking the absolute value of each encoded low-resolution image before further processing, as indicated in Fig. 1.

The advantage is the possibility to make the EPI trajectory narrower, and thus evolving faster in the phase encoding direction, which reduces the distortion and blur of the image, just like a readout-segmented EPI scan with three shots, but without the need for navigators. Applying phaseless encoding to EPI in the phase encoding direction is theoretically possible, but the gain of k-space speed and the related distortion reduction would not be achieved.

So far, it has been shown that diffusion EPI with phaseless encoding can surpass the resolution limit of a single-shot acquisition and produce artefact-free diffusion-weighted scans of 0.75 mm in-plane resolution on a standard 3T scanner, without the need of navigators or any sacrifice of the sensitivity encoding potential. This time, we validate the utility of this method in a protocol closer to the "everyday" DTI practice, namely in a moderate resolution (1.3 mm) scan which can also be performed with single-shot EPI on the same system and show that phaseless encoding produces less distortion in the images. Additionally, we introduce several improvements of the phaseless encoding method that make it applicable in routine mode. First, the tagging RF pulses are made slice selective and the advantages of this modification in a multi-slice scan are demonstrated. Second, since the tagging modulation inevitably leads to an SNR loss compared to a readout-segmented scan, we analyze the relation between the tagging flip angle and the SNR of the reconstructed image and find the flip angle for which the SNR loss is minimal. We also introduce a new filtering scheme to reduce the particular form of Gibbs ringing that appears with the phaseless encoding. This scheme is more efficient than the previously proposed sinusoidal ramps over the overlapping k-space bands. Finally, a method is proposed to reduce the artefact caused by amplitude fluctuations between consecutive encoding steps. The idea of tagging flip angle optimization with respect to SNR and the improved filtering scheme have been shown in conference abstracts [21,22].

2. Theory and methods

Several improvements of both the tagging preparation and the superresolution reconstruction for the phaseless encoding are described below, including slice selective tagging pulses, an SNR-optimization of the tagging flip angle, an improved anti-ringing filtering scheme and a correction of amplitude fluctuations.

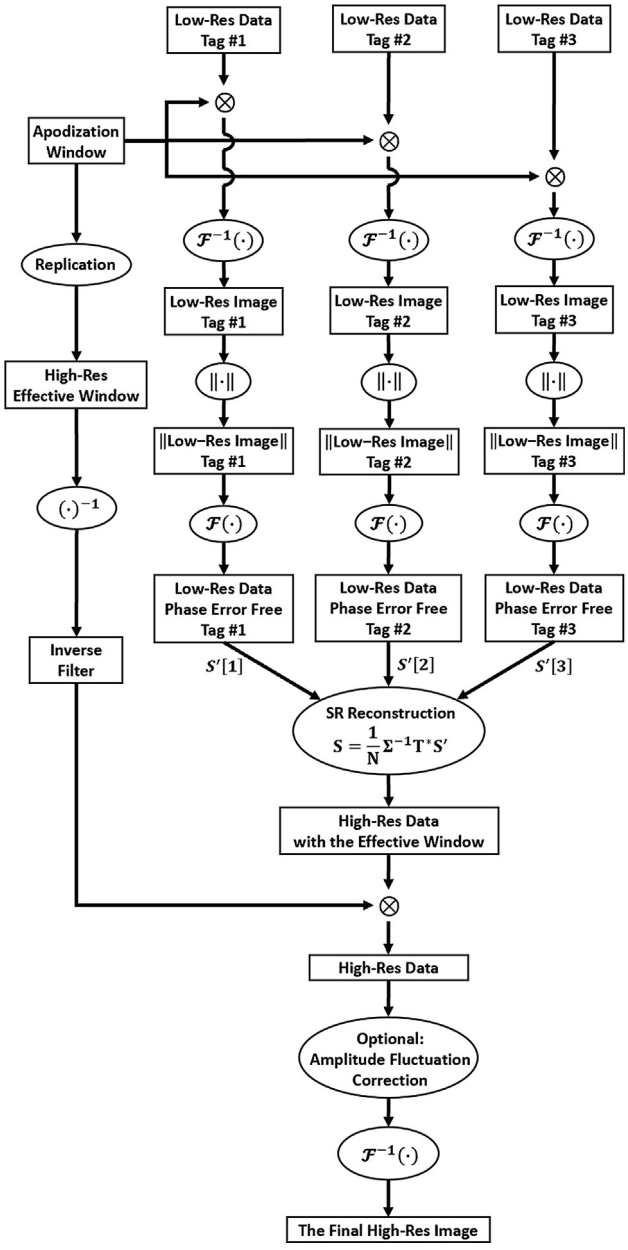

Fig. 1. The flow diagram of the improved phaseless encoding reconstruction. The low-resolution data obtained with three shifts of the tagging modulation are the input to the reconstruction pipeline. They are apodized, magnitude-reconstructed, transformed back to k-space, loaded into the super-resolution reconstruction algorithm, which separates the k-space bands mixed by the tagging, and corrected by the inverse filter leading to the high-resolution data with three-fold resolution enhancement. Optionally, the reconstructed data can be further processed to remove the effect of amplitude fluctuations. Eventually, the final high-resolution image is obtained.

2.1. Slice-selective tagging pulses

In previously described experiments with phaseless encoding, the tagging RF pulses were not slice selective and therefore effective on all slices during the acquisition of each single one. This can lead to "over-tagging" effects, especially with a high number of slices covered during a single repetition time (TR). Here, we analyze these artefacts and their physical origins for different members of a slice package and compare the results to an experiment with slice selective tagging pulses.

A rectangular water-filled phantom containing several silicon tubes (1.5 mm wall thickness) was scanned by multi-slice experiments with 20 slices in total, all excited during a single repetition in two interleaves (1, 3, . . .19; 2, 4, . . .20). Both scans were acquired with gradient echo EPI with the nominal resolution of 2.1 mm (readout, left–right) × 0.75 mm (phase, up-bottom) and reconstructed at the super-resolution of 0.75 × 0.75 mm. The SENSE acceleration factor was 3.0 and the partial-FT factor was 0.625. A two-pulse tagging sequence prior to the EPI sequence produced a sinusoidal pattern with a period of 2.34 mm in the readout direction with 3 shifts (0°, 120°, 240°) in different TR intervals, corresponding to neighboring band overlapping of 10.3%. To visualize saturation effects on the tagging pattern, additional similar scans were taken with a larger pattern period of 15.00 mm but not included in the SR reconstruction. The experiment was conducted with non-slice selective and slice-selective tagging pulses, both with the tagging flip angle 45°, and the time delay between the centers of the two tagging RF pulses 2.5 ms. The slice thickness was 2.0 mm and the gap was 1.0 mm in both scans.

For the slice selective tagging pulses, the waveform of each RF pulse, with a time-bandwidth-product (TBWP) 3.28, was chosen to be asymmetric and thus the second one was time-reversed to minimize the interval between the two flips and the related tag distortions due to field offsets. A compensation gradient lobe was inserted between the two slice selective pulses and the zero-crossing time point of the phase ramp of each pulse was set to coincide with the 'focus' of the respective waveform [23] to prevent any slice-dependent phase shifts of the tagging pattern. The thickness of the tagging pulses was set as 3 mm, which is 1.5 times larger than the one of the excitation pulses, however, without causing the tagging of consecutive slices to overlap.

2.2. SNR-optimized tagging flip angle

Compared to the conventional multi-shot segmented EPI, the signal-to-noise ratio (SNR) in the phaseless encoding is inevitably reduced due to the partial suppression of the signal by the sinusoidal modulation of the longitudinal magnetization. The SNR loss is not "white" and affects the three simultaneously sampled bands in a different manner. As shown in [16], the variance of the reconstructed image, acquired with N pattern shifts and tagging pulse flip angle α, can be expressed by

$$\sigma^2 = \frac{\tilde{\sigma}^2}{3N}\left[\left(\frac{2}{A}\right)^2 + \left(\frac{1}{1-A}\right)^2 + \left(\frac{2}{A}\right)^2\right] \tag{3}$$

where $\tilde{\sigma}^2$ is the variance of a corresponding 3-shot readout-segmented image assuming identical signal noise level, and $A = (\sin\alpha)^2$. The three components in the squared brackets are inverse square amplitudes of the three k-space bands weightings. By calculating the first and the second order derivative of σ^2 with respect to A, it can be shown that the noise propagation in the superresolution image is minimized when $A = \frac{2}{3}$, which corresponds to the tagging flip angle α equal to the magic angle ($\approx 54.74^\circ$). With this tagging angle the contributions of the three bands are equal, the noise spectrum becomes white and its standard deviation equals

$$\sigma = \sqrt{3}\tilde{\sigma} \tag{4}$$

which is significantly better than the noise enhancement of factor 2.0 that was previously obtained with 45° pulses. The tagging pattern produced by a flip angle above 45° reaches negative values in a part of each period and is therefore not strictly phaseless. We assume, however, that such negative lobes are negligible when the tagging flip angle is 54.74° and will not result in negative values of the low-resolution images, which would be inverted by the magnitude operation and could lead to artefacts.

To verify this theory, a series of phantom measurements was carried out using the classic 2D gradient echo sequence (GRE or FLASH). In one scan, which served as an SNR reference, an isotropic k-space region corresponding to 1 mm × 1 mm resolution was covered with the usual frequency- and phase encoding. Further experiments covered only the central 33.3% band of the k-space with the phase encoding, while the frequency encoding range was kept identical giving an effective resolution of 1 mm × 3 mm. These low-resolution scans were repeated with three cycles of phaseless encoding in the direction of the phase encoding, which allowed a reconstruction of the entire k-space range. This setup was intended to mimic a comparison of segmented EPI with phaseless-encoded EPI, but without issues specific to this sequence, like ghosts or distortions. The phaseless encoded scans used tagging flip angles ranging from 25° to 75° and a small (9.7%) band overlapping. The experimentally measured SNR was calculated from the reconstructed superresolution images with various tagging flip angles, as well as from the reference scan, and compared with the theoretical relative SNR computed by the Eq. (3). This analysis used the effective tagging flip angles derived from a measured B1 map, which slightly differed from the scanner's nominal values. The experimentally measured SNR was calculated by taking the ratio between the mean value and the standard deviation of the intensities on a selected uniform area of the phantom.

2.3. Improving the anti-ringing strategy

Before resolving the mixed bands signals, magnitude operation is applied on the low-resolution images to eliminate the phase fluctuation between consecutive tag cycles [15]. This can also invert the negative lobes of the Gibbs ringing, propagating this effect to the final high-resolution image. Therefore, it is important to apply an anti-ringing filter on the low-resolution images to reduce the related artefacts. However, such apodization can result in additional problems. Recall from [16] that the effective k-space window (modulation transfer function) of the phaseless-encoded image is:

$$W_{\text{eff}}(k) = W\left(k - k'\right) + W(k) + W\left(k + k'\right) \tag{5}$$

where W is the anti-ringing window applied to the low-resolution data and k' is the spatial frequency of the tag, i.e. the shift of the simultaneously sampled bands. When the anti-ringing filter is applied, the effective window is periodic and causes ghosting. With partial overlapping of simultaneously excited bands (and a small tradeoff of final resolution), a cosine ramp filter over the overlapped parts of k-space bands could be applied, which adds up to a flat top window. However, the anti-ringing efficiency of this filter was limited, especially, with low overlapping of bands. Therefore, we propose to use optimized anti-ringing filters, such as the Kaiser window to reconstruct the encoded low-resolution images, and compensate their amplitude modulation effect in the reconstructed k-space by an inverse filter:

$$W_{inv} = \frac{W_{\text{hi}}(k)}{W_{\text{eff}}(k)} \tag{6}$$

where W_{hi} is the final desired transfer function extending over the full range of recovered spatial frequencies (rectangular in the simplest case). Division by the effective window is allowed when the bands slightly overlap and the anti-ringing filter is not too strongly apodizing, which is the case for the Kaiser window with the width-parameter alpha set to 3.0, as in all examples presented here. The high-resolution filter W_{hi} was also chosen as the Kaiser window with the width-parameter alpha set to 3.0 but extended over the

full range of the recovered k-space data. The reconstruction based on the inverse filter was tested and compared with the previously described cosine ramp filter strategy.

The proposed filtering strategy was tested with an EPI image from the section of "Slice-selective tagging pulses": the water-filled phantom containing several small silicon tubes acquired with nominal resolution of 2.1 mm (readout, left–right) × 0.75 mm (phase, up-bottom) and reconstructed at the super-resolution of 0.75 mm × 0.75 mm.

2.4. Correcting the amplitude fluctuation between shots

Although phaseless encoding is immune to phase fluctuations of the low-resolution images, it remains sensitive to variations of their magnitude. These may be caused by insufficient stability of the transmission, reception and shim hardware, but also, despite the absolute value calculation, by local variations of signal phase when the images contain residual EPI or SENSE ghosts that interfere with the main image. These amplitude fluctuations can be particularly strong with diffusion weighting. Resulting artefacts have similar intensity as the ghosting observed with such signal variations in interleaved EPI, but their form is different. Instead of ghosts, interference fringes appear in the fluctuating regions [16]. For simplicity, we assume the amplitude fluctuation is location-independent, and the relation between the encoded low-resolution- and high-resolution signals in [16] can be extended by:

$$\mathbf{S}'_{\mathrm{err}} = \Lambda\mathbf{T}\Sigma\mathbf{S} \tag{7}$$

where Λ is a diagonal N-by-N matrix containing the amplitude fluctuation ratios (first diagonal element being 1.0 and remaining ones equal to signal amplitude ratios of further encoding steps to the first one), $\mathbf{T}$ is a N-by-3 matrix of phase coefficients given by the tagging shifts, Σ is a diagonal 3-by-3 matrix containing $(A/2, 1-A, A/2)$ on its diagonal, and $\mathbf{S}$ is a 3-by-1 vector containing unknown signal values in the three bands. The least-squares solution obtained without the knowledge of Λ and thus affected by an error is

$$\mathbf{S}_{\mathrm{err}} = \mathbf{N}^{-1}\Sigma^{-1}\mathbf{T}^{*}\mathbf{S}'_{\mathrm{err}} = \mathbf{N}^{-1}\Sigma^{-1}\mathbf{T}^{*}\Lambda\mathbf{T}\Sigma\mathbf{S} \tag{8}$$

In the presence of the amplitude fluctuation between low-resolution images, i.e. $\Lambda \neq \mathrm{I}$, the term $\mathbf{N}^{-1}\Sigma^{-1}\mathbf{T}^{*}\Lambda\mathbf{T}\Sigma$ remains no longer diagonal and therefore leads to a residual mixing of the original three bands signals in the reconstructed $\mathbf{S}_{\mathrm{err}}$. In particular, the central band signal around the k-space center, which usually has very high intensity, ends up copied (with different scaling) to the central regions of the side bands, giving rise to strong interference fringes with a period of about three pixels.

Therefore, we propose to suppress data points within a small rectangular window (e.g. 21 × 21) around the side band centers, which contribute strongest to the interference fringes. Since the window is quite small compared to the matrix size of the final image (e.g. 192 × 192), the overall image quality and the SNR will not be affected by zeroing these data. This technique was tested on a selected in-vivo diffusion-weighted image in which the interference fringes arise in regions of fat- and ghost-interferences, where motion-induced phase fluctuations affect the magnitude images.

2.5. DTI scans of the human head

Phaseless encoded super-resolution EPI with all improvements described above was applied to acquire multi-slice diffusion images of the human brain and compared to a similar scan using the standard single-shot EPI. All experiments described in this and previous sections were carried out on a 3T MRI system equipped with 30 mT/m, 200 T/m/s gradients (Achieva 3T, Philips Healthcare, the Netherlands) and an eight-channel head array receiver coil using an own modification of the manufacturer's sequence code. In total 15 slices were acquired with the slice thickness of 2.5 mm and the slice gap of 1.0 mm. Two healthy male adults volunteered for the study in agreement with the institution's ethics policy.

The phaseless encoding scan acquired three images with the resolution of 3.44 mm (readout, left–right) × 1.30 mm (phase, up-bottom) and a tagging pattern period of 4.2 mm to reconstruct a high-resolution image with resolution of 1.30 mm in both direction, which corresponds to 18.1% band overlapping. The tagging RF pulses were slice selective with a slightly higher thickness than the excitation (3.5 mm) and their flip angle was set to the magic angle. These acquisitions were all repeated with three shifts (0°, 120°, 240°) of the tagging pattern, with the time delay between tagging RF pulses of 3 ms. The TR (repetition time, counted between excitations of the same slice) was 5 s, which could maximally accommodate an acquisition of 40 slices. The low-resolution data were acquired with the SENSE acceleration factor of 2.0 and a duration of the acquisition window (35 ms) short enough to allow full (symmetric) k-space coverage with an acceptable echo time (81 ms). The B0 maps and B1 maps were acquired by manufacturer's protocols and used to correct the B0- and B1-related tagging distortion [16].

The single shot diffusion weighted spin echo EPI was applied with nominal resolution of 1.30 mm (readout, left–right) × 1.30 mm (phase, up-bottom). It used the SENSE acceleration factor 2.0 and the partial-FT factor of 0.699, leading to a similar echo time (75 ms) despite a longer acquisition window duration (47 ms). For this sequence, the maximum number of slices with the selected TR was 37. Both EPI scans used 30 mT/m readout gradient with a 220 mm × 220 mm FOV corresponding to a signal bandwidth of 280 kHz.

For both scans, the data acquired with EPI were reconstructed off-line using non-Cartesian SENSE and k-space gridding based on a trajectory measured concurrently with a field camera (Skope, Switzerland). The effective k-space windows in both scans were apodized by a Kaiser filter (width coefficient$\alpha = 3.0$) in both dimensions. Isotropic diffusion weighted images were calculated by averaging images obtained with 32 directions of diffusion sensitizing gradients, with b-value 800 s/mm^2. The DTI images were processed using the FSL toolbox [24] to produce the color-coded principle diffusion direction map, with the orientation of the diffusion principle eigenvectors controlling the hue and the fractional anisotropy map controlling the brightness. To compare the signal-to-noise ratio (SNR) of both techniques, non-weighted and diffusion-weighted images (with diffusion gradient along three orthogonal directions) have been repeated 6 times with a different volunteer and the SNR was evaluated for each pixel as the ratio between the mean of the repetitions to their standard deviation.

2.6. Comparison with navigated readout-segmented EPI

The proposed method was also compared with the established navigator-based readout-segmented EPI, implemented on Siemens MRI systems as RESOLVE. One volunteer was examined with 3-shot RESOLVE on a Skyra 3T scanner (Siemens Healthineers, Erlangen, Germany) equipped with 45 mT/m, 200 mT/m/ms gradients, and with the described phaseless encoding approach on the Philips 3T scanner using the same in-plane geometry parameters as previously, 4 mm slice thickness, 3.2 mm gap, 3 orthogonal diffusion directions, b-values 1000 and 2000 ms/mm^2, TR/TE = 4000/100 ms, full k-space sampling, and 4 repetitions to allow an estimation of the signal-to-noise ratio. The RESLOVE-navigator TE was 149 ms. Higher slice thickness was chosen to allow comparison of strongly diffusion weighted images with sufficient SNR. Both scans used an

acceleration factor 2.0, however, in combination with GRAPPA and SENSE on Siemens and Philips scanners, respectively. The phaseless scan was carried out with a different coil (head-and-neck 16-channels), because its geometry was closer to the 20-channel head-array of the Skyra scanner.

3. Results

3.1. Slice selective tagging

When the tagging pulses are not slice selective and the longitudinal relaxation between consecutive tagging sequences is not complete, nonlinear distortions of the tagging pattern take place and produce artefacts in the reconstructed superresolution image. We describe the tagging distortions and the image artefacts based on the experimental results of the slice #17 and the slice #3 respectively, since the physical origin of the tagging imperfections in the slices later in the acquisition order (e.g. the slice #17) may differ from the ones at the beginning (e.g. the slice #3).

The late-acquired slice #17, in which the tagging distortion is simulated in Fig. 2.A1-A2, is saturated by the tagging modulation of other slices in the same tag shift, leading to a tagging pattern narrower than expected in all tagging cycles, as in Fig. 3.A1-A3. As described in the previous simulation study as the "incomplete relaxation" in Fig. S9 in [16], in the k-space, such distorted tagging results in the reduction in the DC component and the emergence of higher order harmonics, which corresponds to the SNR loss (image darkening) and the slight high pass filter effect (small tubes seem to be slightly sharper) in the superresolution image in Fig. 3.A4. On the other hand, the tagging pattern produced by the slice selective tagging pulses is closer to the expected sinusoidal modulation, and therefore the reconstructed superresolution image produces higher SNR without apparent artefacts (Fig. 3.B4).

As shown in Fig. 4, the tagging saturation in the first tag cycle of the early-excited slice #3 (Fig. 4.A1) was similar to the slice #17. However, in the following cycles (Fig. 4.A2-A3) the tagging pattern undergoes further modification and the peak intensity is reduced. This is due to the differently shifted tag from the previous cycle not being completely relaxed. As shown in the simulated pattern in Fig. 2.B1-B2, the result strongly deviates from the sinusoidal waveform and has a reduced DC component. This difference between the tagging patterns in different cycles leads to stripe artefacts (Fig. 4.A4) which are similar to the effect of the signal amplitude changes described in the previous study (Fig. S10 and Fig. S11 in Ref. [16]). On the other hand, the tagging pattern produced by slice selective pulses is free of inter-cycle variations for early slices and the stripe artefacts are absent in the reconstructed superresolution image (Fig. 4.B4).

3.2. SNR vs. tagging flip angle

Super-resolution images obtained with different tagging flip angles are shown in Fig. 5 together with the standard phase-encoded GRE image with identical resolution (image labelled

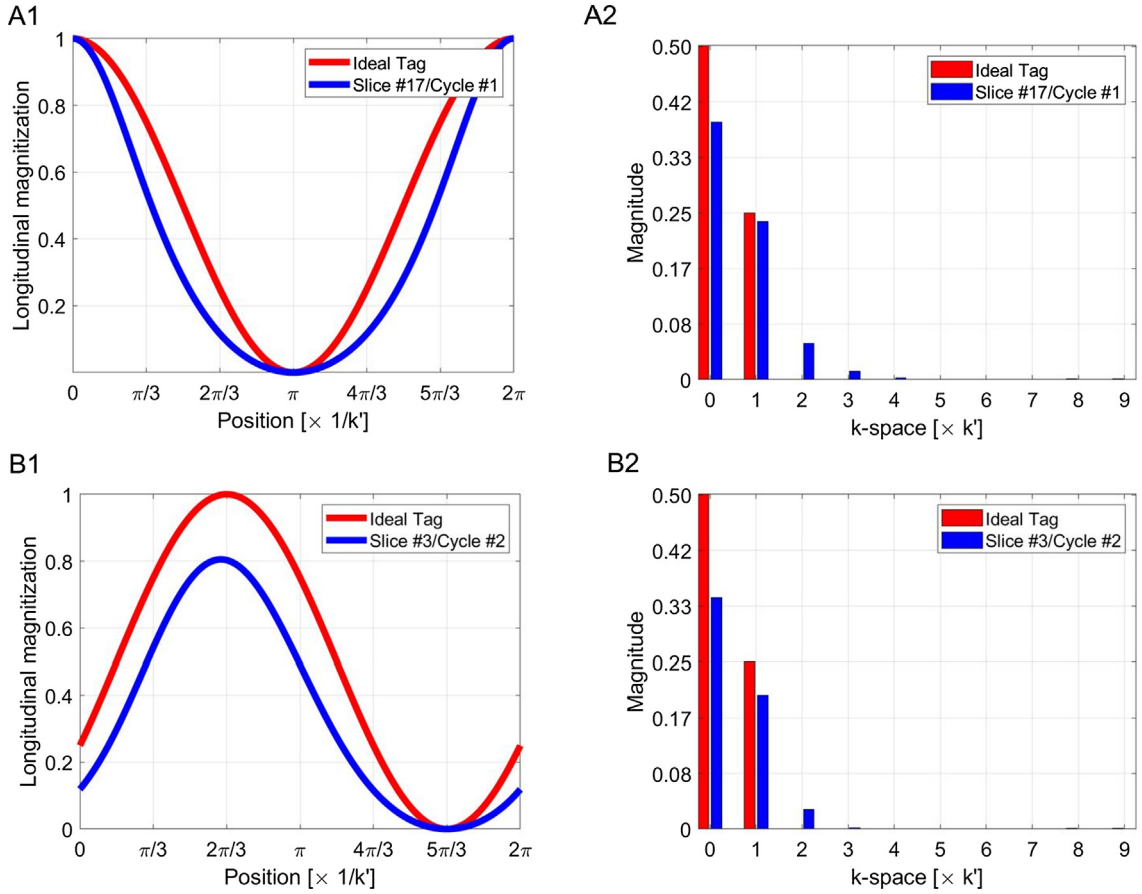

Fig. 2. Simulation of saturated tagging which takes place with non-slice selective tagging RF pulses during multi-slice experiments. In late-excited slices (A), multiple repetitions of the same cycle of the sinusoidal modulation (red curve in A1) leads to flattened tagging pattern (blue curve in A1). In k-space (A2), the energy of the DC component splits into the higher order harmonics. For the early-excited slices, the distortion of tagging pattern (B1, blue curve) is much stronger, since the tagging in the previous cycle is not completely relaxed. This leads to an overall signal intensity reduction and a higher relative contribution of higher harmonics. (For interpretation of the references to color in this figure legend, the reader is referred to the web version of this article.)

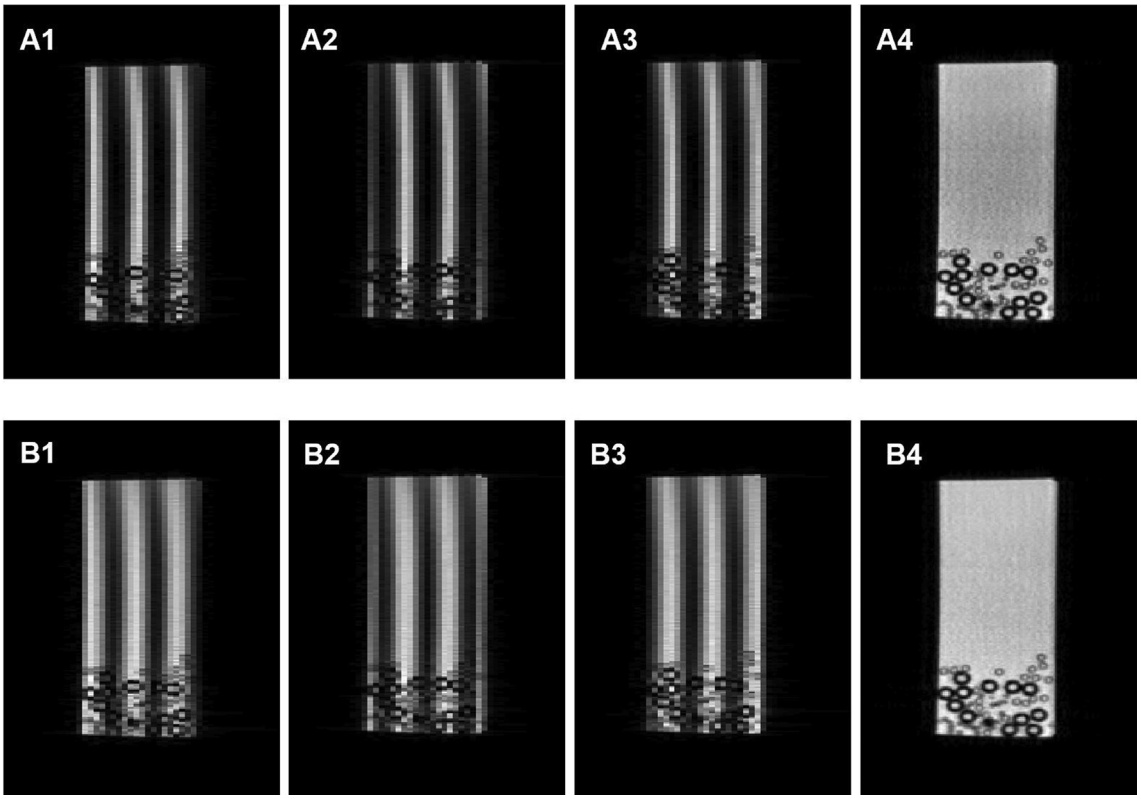

Fig. 3. The slice #17, as one of the late-excited slices, was acquired with non-slice selective (A) or slice selective (B) tagging RF pulses, by a multi-slice experiment on a water phantom with silicon tubes. The column 1–3 represents the low-resolution images in tag cycle from #1 to #3 respectively, with exaggerated tagging wavelength for visualization. The column 4 represents the reconstructed high-resolution image acquired with the correct tagging wavelength. The non-slice selective tagging patterns (A1-A3) end up with narrower tagging width than the slice selective ones (B1-B3), which agrees with the simulation result in Fig. 2A. Consequently, an SNR loss and a slight high pass filter effect can be observed in the reconstructed image with the non-slice selective tagging (A4). No apparent artefacts take place in the reconstruction with the slice selective tagging (B4).

'REF'). The SNR and the spectral contents of the noise is visibly dependent on the tagging flip angle. Quantitative comparison of the SNR of SR-images relative to the GRE reference is presented in Fig. 6 along with the plot of the theoretical value based on Eq. (3).

As seen in both Fig. 5 and Fig. 6, the tagging flip angle of 54.4° (experimental point closest to the magic angle) produced the highest relative SNR of approximately 60% of the SNR of the reference image, which matches the theory quite closely. Although the tagging pattern with this tagging flip angle can reach negative values in a small part of its period, no apparent artefacts is visible in the reconstructed image.

The relative SNR of phaseless encoding decreases more rapidly with the tagging flip above the magic angle than below this value. In addition, when the tagging flip angle is 72.0°, artefacts appear near the phantom contours. These can be attributed to the tagging pattern deviating too far from the assumed "phaselessness": the negative pattern lobes invert the image phase, which is then falsified by the magnitude operation. Therefore, when the flip angle is not precisely controlled, e.g. when the B1 field in inhomogeneous, this result speaks for setting the tagging flip angle slightly below the magic angle to stay on the safe side.

3.3. Improved anti-ringing filtering

A comparison of super-resolution images acquired with identical band overlapping (~10.3%) and reconstructed with different anti-ringing filtering schemes is shown in Fig. 7. The ringing suppression is better with the Kaiser filter associated with the inverse filter described above than with the cosine ramp filter, which is not effective enough with the low overlapping. The new strategy thus has the advantage of allowing the reduction of band overlapping to the very minimum needed to avoid k-space gaps in the case of tagging distortions caused by field inhomogeneity.

3.4. Correction of artefacts caused by amplitude fluctuation

The artefacts due to the amplitude fluctuation were not observed in the phantom testing but sometimes appeared in the in-vivo measurements with diffusion weighting where residual SENSE- or EPI ghosts were not fully suppressed. Their interference with the main image changes from one encoding step to another due to underlying phase fluctuations and leads to strong effective amplitude variations (up to 20% peak-to-peak in the case chosen here) and causes a clear appearance of the mentioned fringe artefact (Fig. 8A). As expected, the proposed suppression of two regions of 21x21 data points around the side bands centers suppresses the artefacts effectively (Fig. 8B). Since this corresponds to discarding only about 3% of the total data, there is no significant tradeoff in image quality.

3.5. DTI of the human head

A comparison of the phaseless encoded DTI-EPI scan with a single shot DTI-EPI with identical resolution and diffusion weighting scheme is presented in Fig. 9.

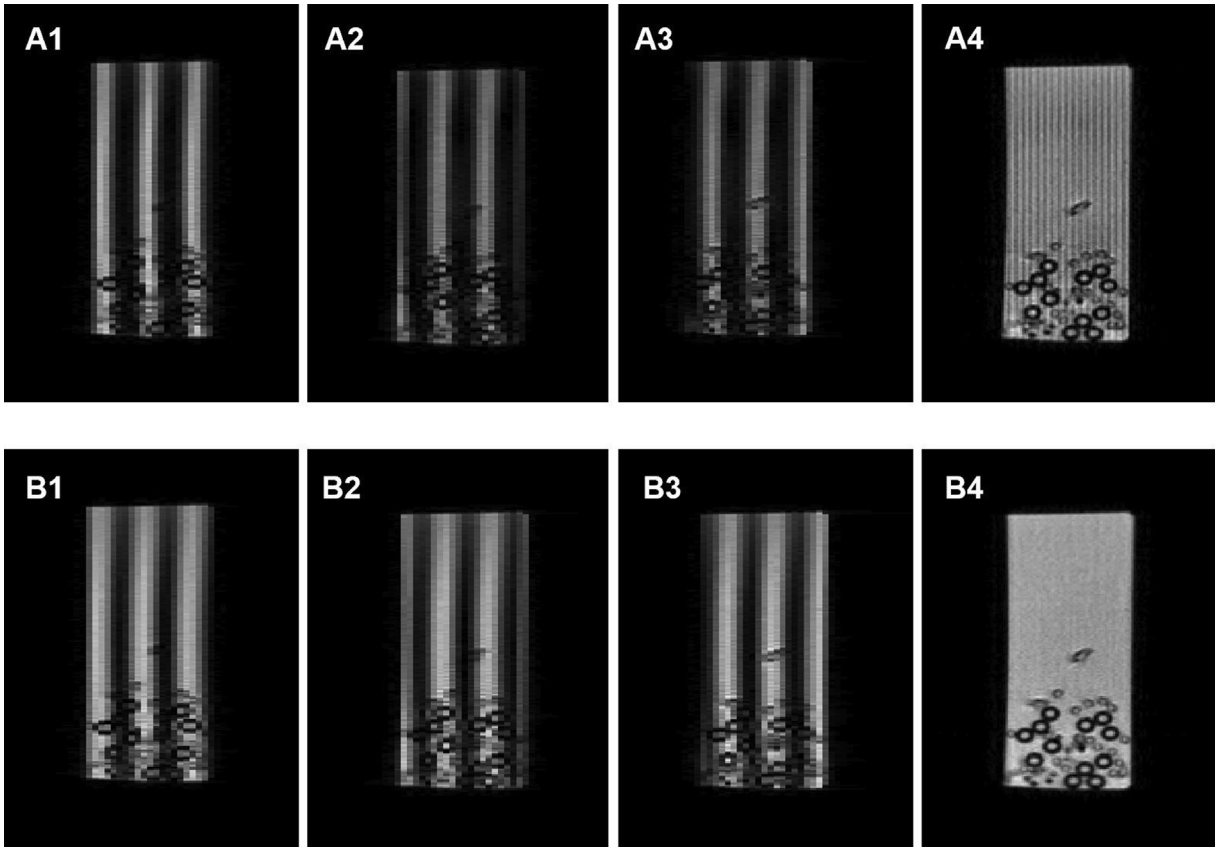

Fig. 4. The slice #3, as one of the early-excited slices, was acquired by either non-slice selective (A) or slice selective (B) tagging RF pulses, from the same multi-slice experiment as in Fig. 3. The column 1–4 are organized in the same way as in Fig. 3. In addition to the narrower tagging width in A1-A3, the non-slice selective tagging introduces strong signal intensity drop in the tag cycle #2 (A2) and #3 (A3), corresponding to the simulation in Fig. 2.B. As expected, the interference fringes appear in the reconstructed image (A4), while no obvious artefacts produced in the slice selective tagging (B1-B4).

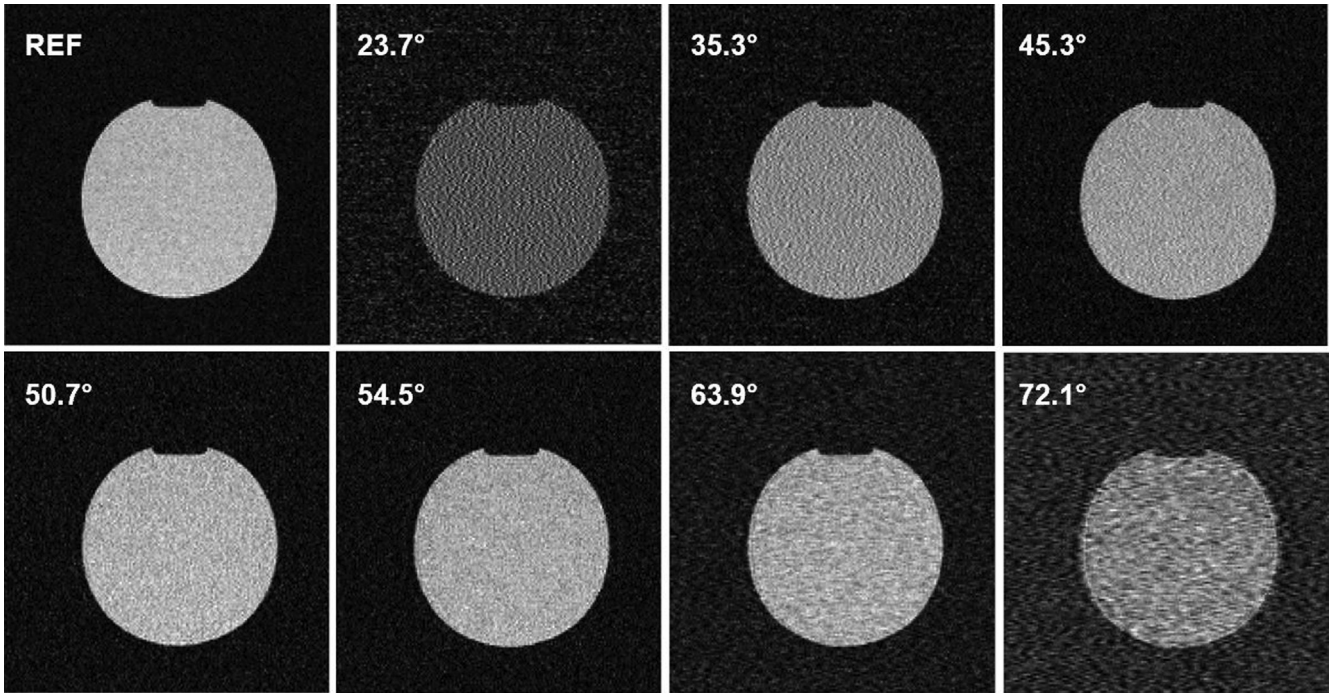

Fig. 5. A gradient echo reference image (REF) compared to phaseless-encoded images obtained with different flip angles of the tagging pattern. The best SNR and the 'white noise' of the phaseless encoded image are achieved close to the magic angle tag (54.7°). Below this angle, high frequencies dominate in the noise because of strong weighting applied during reconstruction to the weakly excited outer k-space bands. With higher flip angles, the noise has dominant low frequency components because the over-represented outer bands are damped by the reconstruction. Additionally, ringing effects appear near the contours with highest flip angles, because the tagging pattern has strong negative lobes and loses its phaseless character.

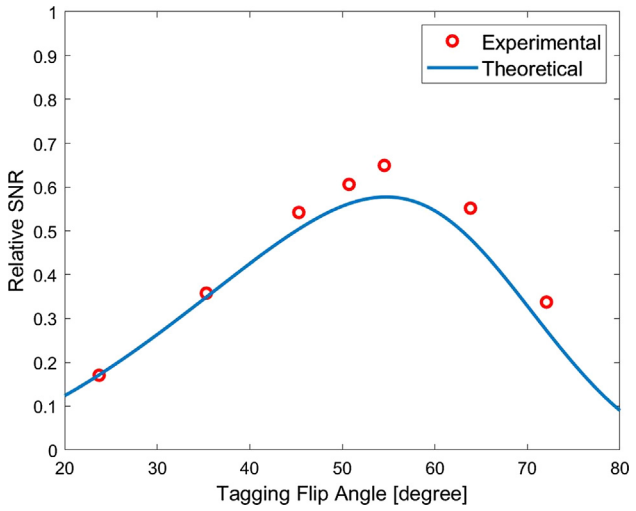

Fig. 6. The SNR of phaseless encoding as a function of the tagging flip angle, relative to the multi-shot segmented scan (mimicked by the GRE scan). The experimental data (red dots) were calculated from the scans in Fig. 5. The theoretical dependency of the relative SNR was computed by the Eq. (3). The relative SNR of the phaseless encoding reaches maximum around the magic angle tagging flip. (For interpretation of the references to color in this figure legend, the reader is referred to the web version of this article.)

A non-weighted spin-echo image, a diffusion-weighted image (sum of images with 32 diffusion gradient directions) with isotropic resolution and the color-coded map of the diffusion tensor's principal eigenvector are presented for one of the 15 slices acquired in both scans. Images were purposely reconstructed without unwarping of field map-related distortions to demonstrate the intrinsic distortion level of both techniques. Both images were identically filtered with a Kaiser 3.0-window in both dimensions. The distortions are substantially reduced in the phaseless encoding scan due to the shorter echo spacing in low-resolution scans. The SNR is only slightly reduced with phaseless encoding despite the mentioned incomplete usage of available signal because this loss is partly compensated by the possibility of symmetric k-space sampling at a comparable echo time that is due to the reduced echo train length (the single-shot scan had to use partial-k-space sampling). The effective resolution of both scans is not visibly different. It should be added, however, that the phaseless encoded scan took three times longer than the single-shot, which is the same as the multi-shot segmented scan. The average SNR value for the central part of the non-weighted brain image derived from the scan with 6 repetitions is 25 for single-shot EPI and 22 for the phaseless encoded EPI. For the diffusion-weighted images, the SNR values are 14 and 11, respectively.

3.6. Comparison with readout segmenting

Images of approximately the same transverse slice of the brain of another male volunteer acquired with the 3-shot, navigated readout segmenting EPI (RESOLVE method) and with the three-step phaseless encoded super-resolution EPI, without and with diffusion weighting in three directions and two different b values, are shown in Fig. 10. All images represent an average of four repetitions. Additionally, each of the repetitions of the non-weighted images was reconstructed separately and used to evaluate the SNR maps for both techniques as a ratio of mean to standard deviation (shown in color).

4. Discussion

Obtaining high-resolution images from a series of magnitude-reconstructed, low-resolution single-shot scans is an attractive alternative to classic multi-shot MRI methods due to the straightforward elimination of the inter-shot phase error problem. However, the phaseless encoding necessary for this approach, which consists of a sub-pixel tagging sequence and corresponds to the optical structured illumination, requires several trade-offs. Unlike the standard phase encoding, it involves manipulation of the longitudinal magnetization and has longer-lasting consequences. A phaseless encoding step (saturation of a tagging pattern) cannot be simply "rewound" before the next one, and has to be given time to relax. This is particularly problematic in multi-slice experiments, where the tagging sequence is repeated multiple times within a single relaxation period (TR). We have shown that the slice selective tagging sequence provides a significant improvement in such scans: the SNR loss caused by multiple repetitions of identical tagging patterns in late-excited slices is reduced and stripe artefacts due to residual shifted tags in early slices are eliminated. However, careful implementation of RF pulse phase ramps and of the selection/compensation gradients is necessary, and the resulting tagging sequence duration becomes longer which may result in higher off-resonance-related errors. These however, can be corrected for based on a magnetic field map, as described before [16].

Another consequence of the encoding based on z-magnetization is the reduction of the available signal. With this regard, the result of the analysis of the SNR as a function of the tagging flip angle appears quite important, because it allows increasing the SNR relative to a standard-segmented scan from $1/2$, which was obtained before with 45° pulses, to $1/\sqrt{3}$ when the flip angle is set to the optimum. The fact that this optimum flip angle happens to be the well-known magic angle that nulls dipolar interactions is a purely coincidental but pleasing surprise as it gives this famous number another application in the domain of magnetic resonance. It should be noted that our analysis assumes that the flip angle used for the reconstruction (via the elements of Σ in Eq. (8)) was effectively applied for the tagging. A deviation from this situation will change the proportions of reconstructed bands and may affect the resulting SNR, which may explain the slight systematic deviation of measured points from the theoretical curve in Fig. 6.

The proposed anti-ringing filtering process allows using optimized apodization windows on the low-resolution data and can easily get rid of the replicated filter window in the high-resolution data. This allows working without unnecessarily high band overlaps (and resolution reduction) that were needed for the sole purpose of ringing suppression with the previously used sine-ramps. Only a very limited band-overlapping is still needed to prevent holes between the k-space bands in realistic situations. It should also be noticed that the band-overlapped regions may have higher SNR due to the averaging of different band signals. This, however, has little impact on the overall SNR and was neglected in the presented SNR analysis. Finally, the proposed amplitude fluctuation correction works well in practice and can be considered as a standard procedure for the method to avoid any unwanted interference fringes due to the amplitude variations between consecutive excitation steps.

It should also be noted that phaseless encoding with the resolution enhancement beyond three is also possible as demonstrated in a conference abstract, which might allow further shortening of the

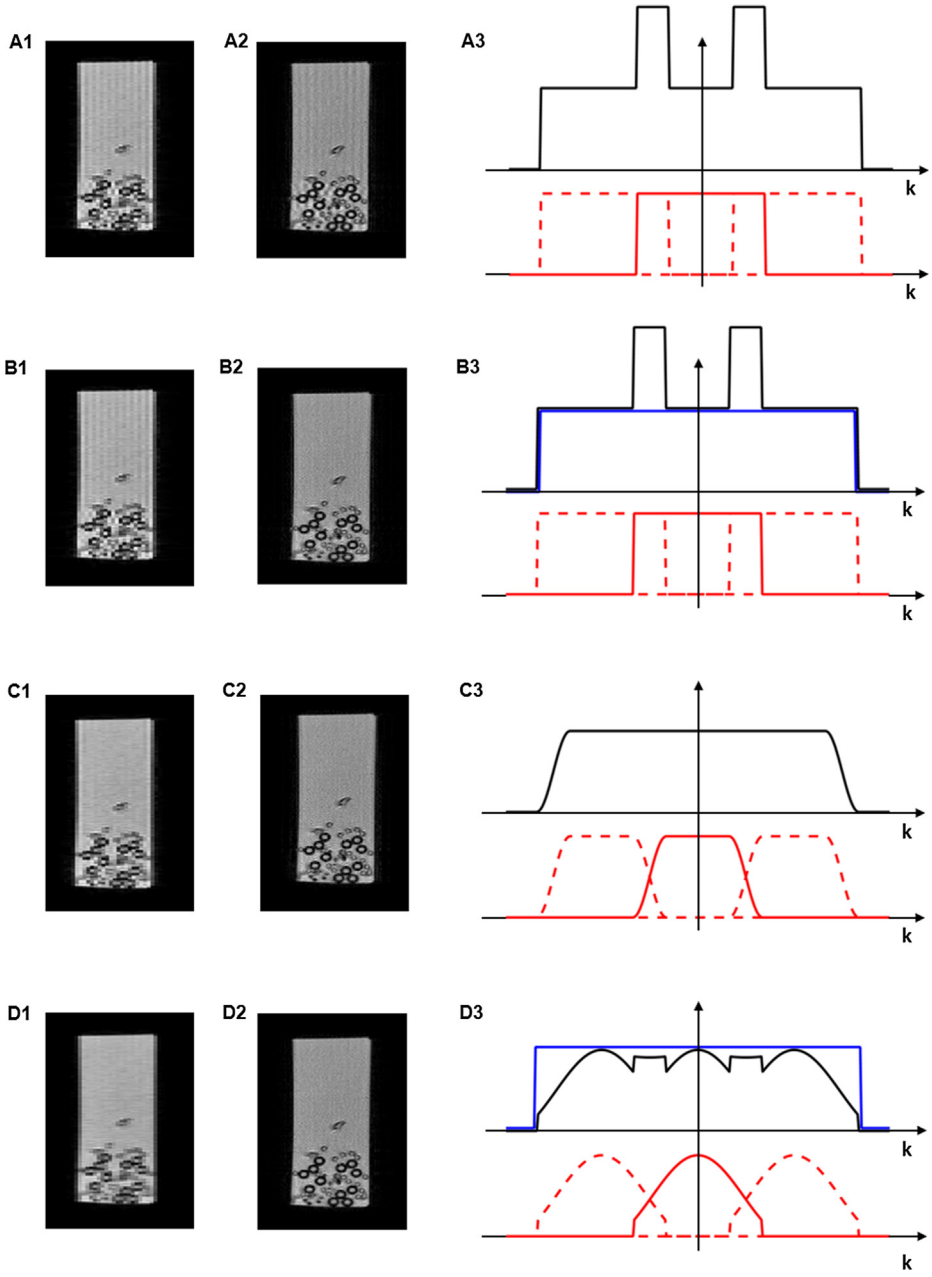

Fig. 7. Improved anti-ringing filtering. Column 1 represents low-resolution images reconstructed with different k-space apodizations (one of the three tagging cycles). The column 2 represents the reconstructed high-resolution images. Column 3 represents the effective high-resolution k-space window (black line) which results from summing up the low-resolution apodization window (solid red) and its replicas (dashed red). Without apodization (row A) the effective window is strongly modulated due to band overlapping and leads to strong ringing. This effect is reduced by the inverse filter which makes the effective window flat (row B, blue line), but residual ringing remains due to the unsuppressed Gibbs ringing in the input images. With the sine ramp apodization used previously (row C), the final filter is flat and does not need corrections. However, residual ringing can still be observed due to limited efficiency of the ramp filter. The improved strategy (row C) is based on the Kaiser filter, which provides better ringing suppression on the low-resolution images and on the final super-resolved image. However, this filter leads to a modulated accumulation of the replica (black line in D3) and needs to be corrected by an inverse filter to achieve a flat effective k-space window (blue line). (For interpretation of the references to color in this figure legend, the reader is referred to the web version of this article.)

echo train [21]. However, this is usually not as efficient as the echo train reduction in the three-fold superresolution case due to gradient slew-rate limits. In this case, applying phaseless encoding in two orthogonal dimensions can be more efficient, but stronger SNR loss will take place due to the signal modulation along two spatial dimensions.

The comparison of phaseless encoding with RESOLVE, carried out with different scanners and different receiver coils should only be treated qualitatively. However, it shows that both methods deliver apparently equivalent data, and the slight reduction of the SNR inherent to the phaseless encoding is an acceptable tradeoff for its ability to measure high-resolution diffusion MRI data in multiple shots without the need of navigators. This advantage may be explored in experiments where navigators are problematic due to low signal or to the extra RF power deposition they require.

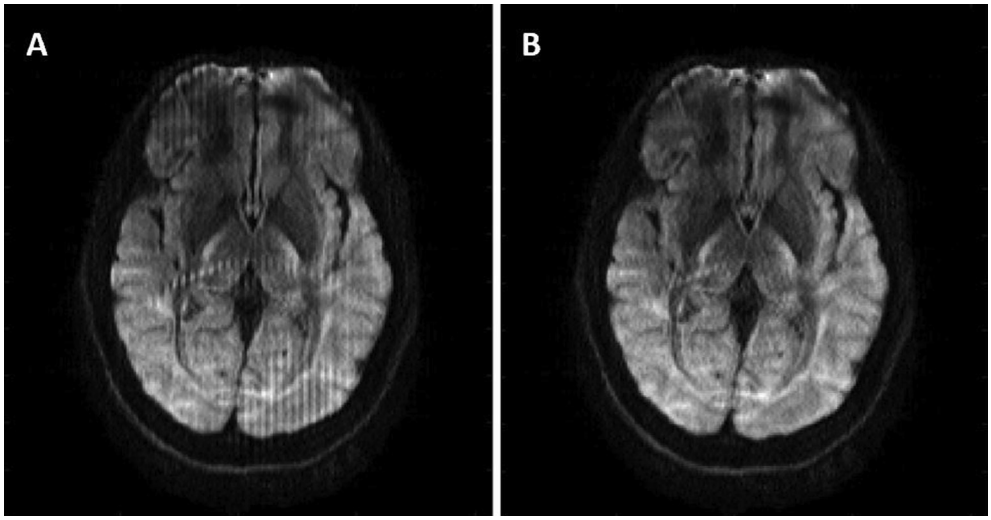

Fig. 8. Amplitude modulation effects. When the signal amplitude changes between the phaseless encoding cycles, the super-resolved image contains interference fringes due to the partial propagation of the central k-space band to the sidebands, as shown here for the spin echo EPI (A). This effect can be largely reduced by zero-filling of small k-space regions around the sideband centers.

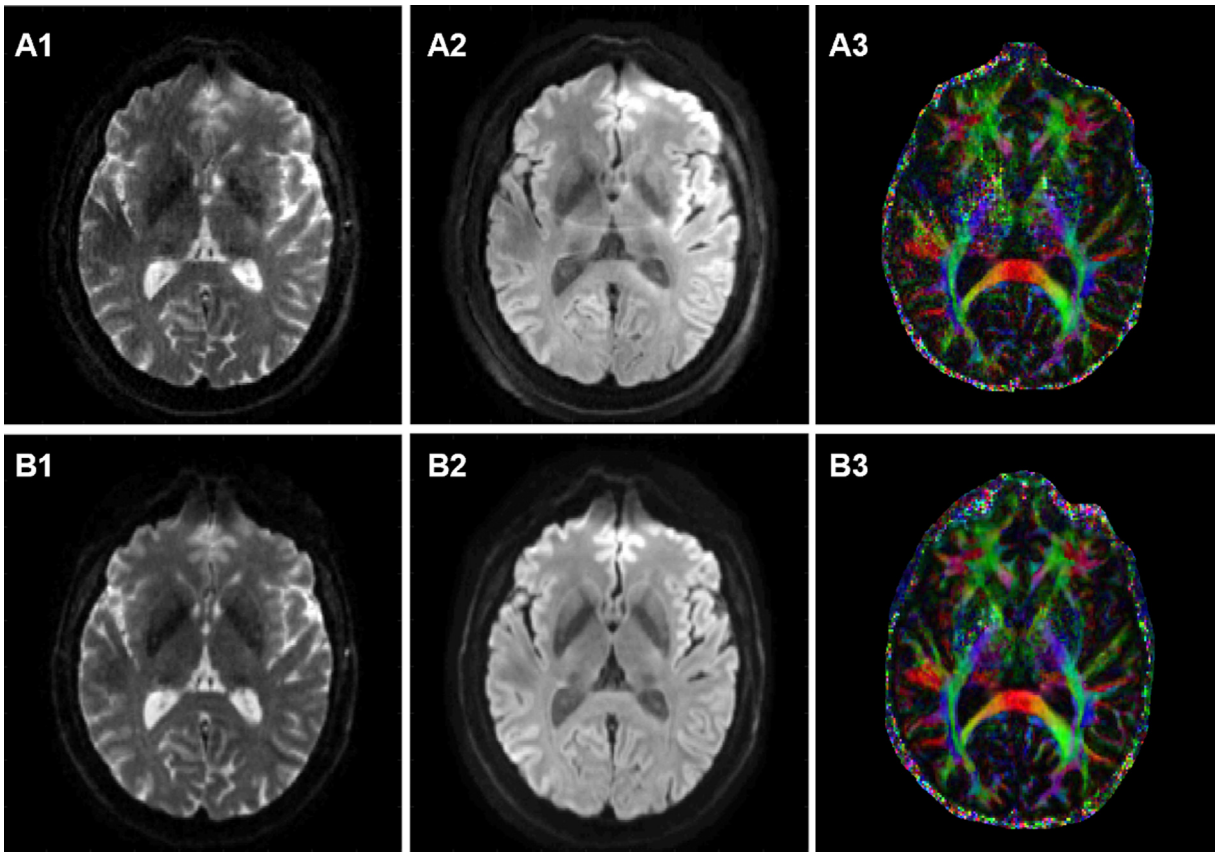

Fig. 9. The DTI comparison between the phaseless encoding EPI with 3 cycles (A) and the single-shot EPI (B) with identical resolution (1.3 mm × 1.3 mm). The column 1 represents the unweighted spin-echo images. The column 2 represents the sum of the diffusion-weighted images in 32 directions. The column 3 represents the color-coded map of the principle eigenvector of the diffusion tensor. A reduced image distortion in regions of magnetic field inhomogeneity (e.g. in the frontal lobe) is observed with the phaseless encoding due to the decreased echo spacing needed for the low-resolved tagged scans used in this technique. The SNR related to the phaseless encoding is partly compensated by the reduction of echo time, which is allowed by shorter echo train length of the low-resolution scans.

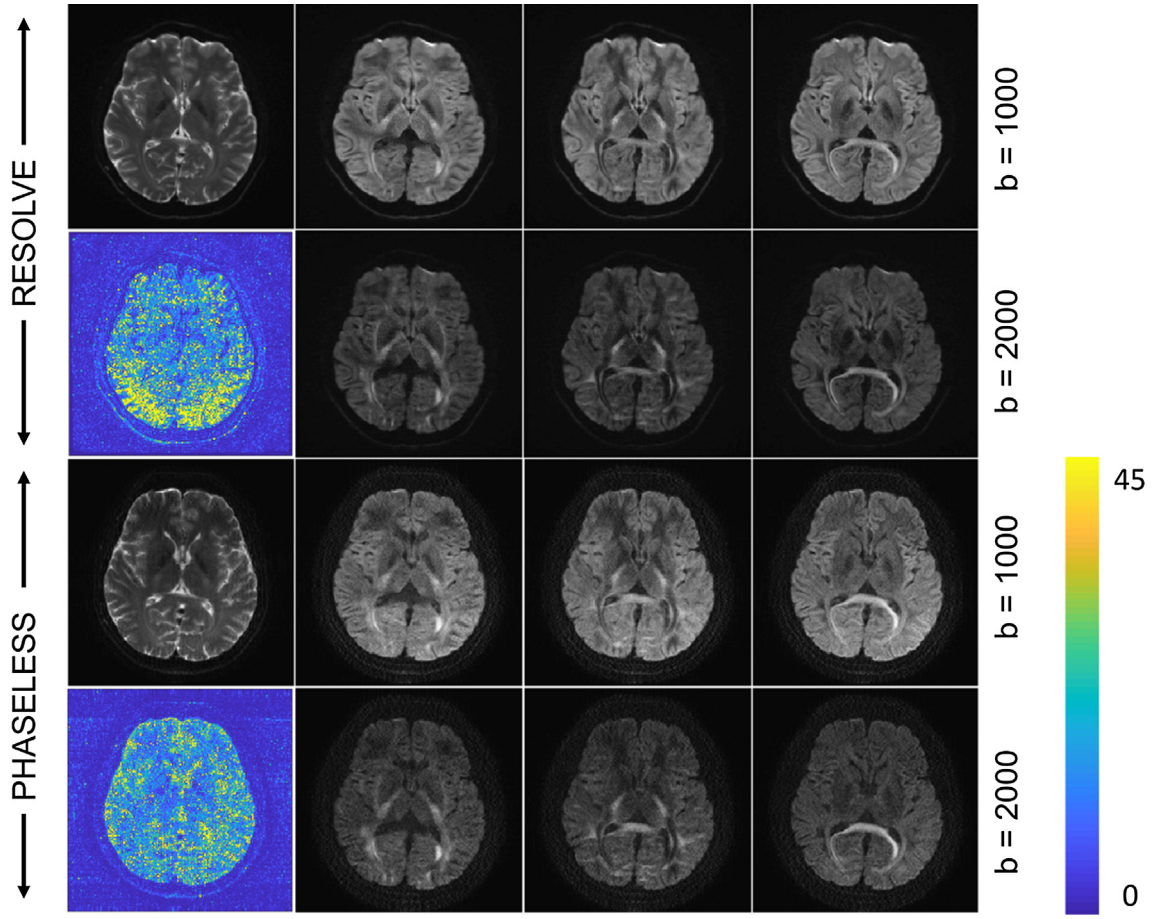

Fig. 10. Comparison of the readout segmented navigator-based EPI (RESOLVE) with phaseless encoding EPI acquired for the same volunteer on two different scanners. A non-weighted image and its SNR map (color scale) is shown in the first column; further columns contain images with diffusion weighting in the left-right, posterior-anterior and head-feet directions with two b-values (s/mm^2).

5. Conclusions

Super-resolution MRI based on phaseless encoding proves to be a promising alternative to multi-shot segmented scans when the signal phase is unstable, e.g. with diffusion weighting. Similar to the segmented multi-shot techniques, it can be used not only to reach higher spatial resolution, but also to achieve shorter echo time and lower distortions than a single shot scan with given gradient constraints. With the proposed optimization of the tagging sequence and of the reconstruction procedure, the phaseless encoding method makes a significant step towards routine clinical usage. This is illustrated by the presented multi-slice DTI-EPI scan of the human head with 1.3 mm in-plane resolution in which the spatial distortion is significantly reduced compared to a similar scan based on single-shot EPI while the artefacts due to motion-induced inter-shot phase variations are absent.

Declaration of Competing Interest

Klaas P. Pruessmann holds a research agreement with and receives research support from Philips Healthcare. He is a shareholder of Gyrotools LLC and Skope Magnetic Resonance Technologies AG.

Acknowledgements

The authors are grateful to Dr. Cristina Rossi of the University Hospital Zurich and Dr. Markus Klarhoefer of Siemens Switzerland for their precious help in scanning with the Siemens system.

References

[1] M.K. Stehling, R. Turner, P. Mansfield, Echo-planar imaging: magnetic resonance imaging in a fraction of a second Oct 4 Science 254 (5028) (1991) 43–50.
[2] D.G. Norris, Implications of bulk motion for diffusion-weighted imaging experiments: Effects, mechanisms, and solutions, J. Magn. Reson. Imaging 13 (4) (2001) 486–495.
[3] P. Jezzard, R.S. Balaban, Correction for geometric distortion in echo planar images from B0 field variations, Magn. Reson. Med. 34 (1) (1995) 65–73.
[4] H. Chang, J.M. Fitzpatrick, A technique for accurate magnetic resonance imaging in the presence of field inhomogeneities Sep IEEE Trans. Med. Imaging 11 (3) (1992) 319–329.
[5] K.P. Pruessmann, M. Weiger, M.B. Scheidegger, P. Boesiger, SENSE: Sensitivity encoding for fast MRI, Magn. Reson. Med. 42 (5) (1999) 952–962.
[6] G.C. McKinnon, Ultrafast interleaved gradient-echo-planar imaging on a standard scanner, Magn. Reson. Med. 30 (5) (1993) 609–616.
[7] M.D. Robson, A.W. Anderson, J.C. Gore, Diffusion-weighted multiple shot echo planar imaging of humans without navigation, Magn. Reson. Med. 38 (1) (1997) 82–88.
[8] A.W. Anderson, J.C. Gore, Analysis and correction of motion artifacts in diffusion weighted imaging, Magn. Reson. Med. 32 (3) (1994) 379–387.
[9] S.J. Holdsworth, S. Skare, R.D. Newbould, R. Guzmann, N.H. Blevins, R. Bammer, Readout-segmented EPI for rapid high resolution diffusion imaging at 3T Jan Eur. J. Radiol. 65 (1) (2008) 36–46.
[10] K. Butts, J. Pauly, A.D. Crespigny, M. Moseley, Isotropic diffusion-weighted and spiral-navigated interleaved EPI for routine imaging of acute stroke, Magn. Reson. Med. 38 (5) (1997) 741–749.
[11] D.A. Porter, R.M. Heidemann, High resolution diffusion-weighted imaging using readout-segmented echo-planar imaging, parallel imaging and a two-dimensional navigator-based reacquisition Aug Magn. Reson. Med. 62 (2) (2009) 468–475.
[12] N. Chen, A. Guidon, H.-C. Chang, A.W. Song, A robust multi-shot scan strategy for high-resolution diffusion weighted MRI enabled by multiplexed sensitivity-encoding (MUSE) May NeuroImage 15 (72) (2013) 41–47.
[13] M.-L. Chu, H.-C. Chang, H.-W. Chung, T.-K. Truong, M.R. Bashir, N. Chen, POCS-based reconstruction of multiplexed sensitivity encoded MRI (POCSMUSE): a

general algorithm for reducing motion-related artifacts Nov Magn. Reson. Med. 74 (5) (2015) 1336–1348.
[14] T.-K. Truong, A. Guidon, High-resolution multi-shot spiral diffusion tensor imaging with inherent correction of motion-induced phase errors Feb Magn. Reson. Med. Off. J. Soc. Magn. Reson. Med. Soc. Magn. Reson. Med. 71 (2) (2014) 790–796.
[15] F. Hennel, K.P. Pruessmann, MRI with phaseless encoding, Magn. Reson. Med. 78 (3) (2017) 1029–1037.
[16] F. Hennel, R. Tian, M. Engel, K.P. Pruessmann, In-plane "superresolution" MRI with phaseless sub-pixel encoding, Magn. Reson. Med. 80 (6) (2018) 2384–2392.
[17] S. Ropele, F. Ebner, F. Fazekas, G. Reishofer, Super-resolution MRI using microscopic spatial modulation of magnetization Dec Magn. Reson. Med. 64 (6) (2010) 1671–1675.
[18] Rainer Heintzmann, Christoph G. Cremer, Laterally modulated excitation microscopy: improvement of resolution by using a diffraction grating, in: Proc. SPIE 3568, Optical Biopsies and Microscopic Techniques III, (19 January 1999); https://doi.org/10.1117/12.336833.
[19] M.G.L. Gustafsson, Surpassing the lateral resolution limit by a factor of two using structured illumination microscopy, J. Microsc. 198 (2) (2000) 82–87.
[20] J.T. Frohn, H.F. Knapp, A. Stemmer, True optical resolution beyond the Rayleigh limit achieved by standing wave illumination Jun 20 Proc. Natl. Acad. Sci. 97 (13) (2000) 7232–7236.
[21] R. Tian, F. Hennel, K.P. Pruessmann, Exploring the limits of super-resolution MRI with phaseless encoding, in: Proceedings of the Joint Annual Meeting of ISMRM-ESMRMB 2018, Paris, France. Program # 2671.
[22] R. Tian, F. Hennel, K.P. Pruessmann, Super-resolution MRI with 2D phaseless encoding, in: Proceedings of the Annual Meeting of ISMRM 2019, Montreal, Canada. Program # 4675.
[23] F. Hennel, The effective phase of soft RF pulses: Effective phase of soft RF pulse Jul Concepts Magn. Reson. Part A 43 (4) (2014) 127–137.
[24] M. Jenkinson, C.F. Beckmann, T.E.J. Behrens, M.W. Woolrich, S.M. Smith, FSL Aug NeuroImage. 62 (2) (2012) 782–790.